Metallography, Microstructure, and Analysis (2023) 12:1009–1019
https://doi.org/10.1007/s13632-023-01006-5

ORIGINAL RESEARCH ARTICLE

Influence of Various Alloying Element Additions on Microstructure and Magnetic and Mechanical Properties and Corrosion Behavior of Cast Fe–Ga–Z Shape Memory Alloys

Nader El-Bagoury[1] · Shimaa El-Hadad[1] · Madiha Shoeib[1]

Received: 12 May 2023 / Revised: 2 September 2023 / Accepted: 24 September 2023 / Published online: 8 November 2023

Abstract
Fe–Ga alloys are attractive materials where high mechanical strength, toughness, ductility, and large low-field magnetostriction combine to give unique properties. Adding alloying elements is an effective method to further enhance these properties. In order to integrate these alloys into the operating environments, e.g., micro-robots and magnetic actuators, the corrosion behavior should be addressed. This work analyzed the microstructure, magnetization, hardness, and corrosion properties of $Fe_{81}Ga_{19-x}Z_x$ ($X = 5$ at.% of Ni, Mn, or Ti, and 2 at.% Al; separately) alloys. X-ray diffraction (XRD), scanning electron microscope-electron (SEM), vibrating sample magnetometer (VSM), Vickers hardness (HV), and a potentiostat were used for characterization. XRD revealed that the prominent peak belongs to the bcc disorder A2 phase and a small peak for the cubic order $L1_2$ phase. Fe–Ga–Al alloy got the maximum Ms value, while Fe–Ga–Mn alloy gained the lowest one. However, the Mr and Hc properties for Fe–Ga alloy were distinctly improved by adding Al but slightly affected by doping Mn. Addition of Ti achieved the highest hardness, followed by Ni, Mn, and Al. The microstructure of the different alloys significantly influenced their corrosion behavior. Fe–Ga–Mn alloy with the fine globular grain structure showed the lowest corrosion rate (C R = 0.03 mm/year), whereas Fe–Ga–Al alloy with the coarse longitudinal grains exhibited the highest corrosion rate (C R = 0.19 mm/year).

Keywords Fe–Ga shape memory alloys · XRD · Microstructure · Magnetization · Corrosion

Introduction

Magnetostrictive materials, including Fe–Ga alloys, are functional materials whose main feature is the interaction of the magnetic and crystalline structure (magneto-mechanical interaction) when an external magnetic field or mechanical stress is applied. The magnetic properties of Fe–Ga alloys have been known for more than 50 years [1–5], but interest in them sharply increased about 20 years ago. Ferromagnetic alloys developed in the USA in the early 2000s are based on the Fe–Ga binary system (galfenol, an abbreviation from gallium, ferrum, and NOL, i.e., the Naval Ordnance Laboratory [2]) and have record-breaking saturation magnetostriction (up to 400 ppm in single crystals) among iron-based alloys. Galfenols are an alternative to the Terfenol-D alloy with a high content of rare earth elements ($Tb_{0.3}Dy_{0.7}Fe_2$), which has poor mechanical properties [1, 6–8]. Due to the successful combination of functional and mechanical properties, Fe–Ga alloys are used for the manufacture of pressure indicators, sensors, and sonars. The low-temperature diffusion-controlled phase transformations proceed slowly in this system's alloys, allowing one to maintain non-equilibrium high-temperature phases formed after crystallization from the melt or quenching at room temperature. The best functional properties in galfenols are achieved with a Ga content of about 19 or 27 at.%. However, not only are these properties determined by the composition, but also highly rely on the conditions of processing the alloys; moreover, they can also be improved by micro-alloying with rare earth elements [9]. By increasing the content of Ga in Fe–Ga alloys, their structure becomes more complex, and a whole cascade of first-and second-order phase transformations, including the formation of both disordered (A1, A2, and A3) and ordered (B2, D03, $L1_2$, L60, D019, and D022) structures, takes place

✉ Nader El-Bagoury
nader_elbagoury@yahoo.com

[1] Central Metallurgical Research and Development Institute, CMRDI, PO Box 87, Helwan, Cairo, Egypt

under thermal influences [10, 11]. Although Fe–Ga alloys with high magnetostriction values have already been used in electronic devices, the physical reasons for their functional properties are not entirely understood or interpreted. Despite the submitted efforts for over 20 years, the primary sources for the distinguished giant magnetostriction in Fe–Ga alloys are still widely ambiguous. There remains no unmysterious information about the causes what for the magnetostriction of nonmagnetic Ga so spectacularly elevates in Fe alloys.

Additionally, why there are two maxima are noticed in the reliance of the magnetostriction constant on the Ga amount at 19 and 27 at.% Ga. This shortcoming is associated with a need for more structural and microstructural data at the atomic level and a lack of knowledge about the occurrence of phase transformations in heating, cooling, and isothermal exposure. Even though revealing a lot of characteristics of phase transformations in galfenols, the use of a traditional set of metallurgical techniques, such as metallographic analysis, scanning and magnetic force microscopy, magnetic vibrometry, calorimetry, dilatometry, and mechanical tests, did not help to answer the question about the origin of high magnetostriction.

GOLOVIN et al., accordingly [12], to solve these problems, it is helpful to apply experimental methods with which the missing structural data could be obtained. In recent years, high-resolution transmission electron microscopy (HRTEM), synchrotron x-ray diffraction (XRD), and neutron diffraction (ND) methods have been used to study the structure of bulk alloys and thin films based on galfenols. The use of these techniques made it possible not only to study the fine structure of cast and heat-processed galfenols and show the features of their surface and bulk structures but also to determine the specifics of their cluster structure and first- and second-order phase transformations in the course of crystallization, quenching, continuous heating and cooling, and isothermal annealing.

Fe–Ga group of alloys is characterized by high mechanical strength, toughness, low cost and, of prime importance, low-field magnetostriction. Such a unique combination of properties makes these alloys good candidates for generators, linear motors, acoustic sensors, actuators, damping devices, torque sensors, etc. Although the literature is full of works that were concerned with the magnetic properties of these alloys, there is almost no study about the corrosion of Fe–Ga alloys except for the research of Tanjore et al [13]. In that work, the corrosion of different single-crystal Fe–*x*Ga alloys in HCl and NaCl solutions were investigated. It was observed that Ga content along with crystal orientation affects the corrosion resistance of the alloys. In the current research, there is a variety of microstructures that are expected to influence the corrosion behavior of the prepared alloys. Therefore, the corrosion resistance of Fe–Ga–X alloys was assessed in 3.5% NaCl solution, which is the most common corrosion media. The results were related to the influence of the third alloying element, "Z" on the microstructure features of the alloy.

The addition of the third alloying elements such as Ni, Mn, Ti, and Al to the Fe–Ga alloy system is of a great importance on influencing the properties of this system such as magnetic, mechanical, and corrosion resistance. For example, in the ternary Fe–Ga–Al alloys, adding Al substitutionally to Ga atoms stabilizes the D03 phase at low temperatures since this phase is stable at room temperature in binary Fe–Al alloy [14]. Moreover, Ni is added to Fe–Ga alloy to form special textures that significantly improve magnetostrictive properties at a certain amount of additives [15]. Additionally, Mn controls the martensitic transformation temperature in Fe–Ga–*x*Mn alloys, it rapidly decreases with increasing x [16]. Finally, Ti presents in "Heusler alloys" to encourage the process of electron spin, for conducting magnetism and ferromagnetic shape memory in spintronics industry [17].

The influence of the addition of various elements such as Ni, Mn, Ti, and Al with various amounts on the microstructure, magnetic, mechanical properties, and corrosion of $Fe_{81}Ga_{19}$ alloy will be investigated in this work.

Experimental Procedures

$Fe_{80}Ga_{20-x}Z_x$ SMAs ($X=5$ at.% of Ni or Mn or Ti and 2 at.% Al; separately) were prepared by vacuum arc melting (VAM) technique under a protective argon atmosphere, where *Z* represented the third alloying element (Z: Ni, Mn, Al, and Ti). The purity of alloying elements used to cast investigated alloys is about 99.99%. These cast alloys were melted many times to ensure homogeneity and to get uniform chemical composition throughout them. They were prepared in a disk shape with dimensions of about 70 mm diameter (f) and 10 mm thickness and weight ranging from 200 to 250 g.

The alloy composition was detected using a foundry master spectrometer, as illustrated in Table 1. The microstructure of cast alloys under investigation was studied by both Meiji optical microscope fitted with a digital camera and the JEOL JSM5410 field emission scanning electron microscope (FESEM). The specimens for microstructure examination were prepared by standard metallographic procedures and then etched in a solution of HNO_3, HF, and H_2O in a ratio of 4:1:5, respectively.

The different phases existing in the structure were analyzed using an energy-dispersive X-ray spectrometer (EDS) attached in the SEM operated at 20 kV. Moreover, X-ray diffraction (XRD) was carried out to identify the different existing phases in the structure using Cu Ka radiation with a step scanning in 2q range of 35–90°. The phase transformations of the cast alloys were measured by Netzsch CC 200

Table 1 Chemical composition of Fe–Ga-studied alloys, at.%

Alloy	At, %					
	Fe	Ga	Ni	Mn	Al	Ti
Fe–Ga–Ni	80	15	5	…	…	…
Fe–Ga–Mn	80	15	…	5	…	…
Fe–Ga–Al	80	18	…	…	2	…
Fe–Ga–Ti	80	15	…	…	…	5

F1 differential scanning calorimeter (DSC) with a cooling/heating rate of 10°Cmin-1in the temperature range from and from room temperature (25 °C) to 1000 °C and from − 90 to 300 °C. Magnetic properties were evaluated using a vibrating sample magnetometer (VSM; lakeshore 7400; USA). Hardness values were determined using a Leco Vickers hardness tester LV800AT with 10 Kg load that applied for 20 s.

The samples for electrochemical tests were cut from each alloy (Fe–Ga–Ni, Fe–Ga–Mn, Fe–Ga–Al, and FeGaTi) at the position next to the microstructure samples. The samples were ground, polished, and cleaned in ultrasonic followed by washing in distilled water and drying. The corrosion behavior of the current specimens was evaluated using a potentiostats instrument (Metrohm AutolabPGSTAT302N). Using software (Nova), which is attached to the instrument, the electrochemical impedance and potentio-dynamic polarization measurements were determined. The electrochemical cell was composed of the anode (sample), cathode (platinum electrode), and reference electrode (Ag/AgCl). The exposed area of the working electrode was 0.35 cm^2, and a 3.5% NaCl solution was used as the liquid media. Initially, the system performs a steady-state open circuit potential (OCP) that ranges between − 0.4 and 0.4 V, and a scan rate of 0.001 V/s was applied. All the tests were performed at room temperature, and the frequency range was between 100 kHz and 0.1 Hz using 0.01 V amplitude. The potential against current plots was obtained along with the impedance plots. The corroded areas of the different specimens were investigated using SEM & EDS.

Results and Discussion

Microstructure Investigations

The microstructure of Fe–Ga alloys is a complex one, and a whole cascade of first- and second-order phase transformations, including the formation of both disordered (A1, A2, and A3), and ordered (B2, D03, $L1_2$, L60, D019, and D022) structures, takes place under thermal influences [1, 4, 10, 11].

The microstructure of Fe–Ga–Ni specimen consists of disordered A2 phase (with short range ordering between Ga–Ga atoms in BCC α iron), as a parent phase, the matrix, and precipitation of $L1_2$ (Fe_3Ga) structure as a second phase. The latter phase precipitated as islands of strips and plate-like shapes, as illustrated in Figs. 1 and 2 that taken by using field emission scanning electron microscope (FESEM).

With higher magnifications, the microstructure of Fe–Ga–Ni specimen is shown in Fig. 2a, as well as the back-scattered image for the microstructure of Fe–Ga–Ni specimen is illustrated in Fig. 2b.

The other 3 specimens of Fe–Ga–Mn, Fe–Ga–Al, and Fe–Ga–Ti have a microstructure that consists of A2 phase as a matrix, just like in case of Fe–Ga–Ni specimen, however, it contains small D03 type ordered clusters [5] due to the doping of the third element such as Mn, Al, and Ti in the Fe–Ga alloy, see Fig. 1b–d, respectively. These fine precipitates are located inside the grains of the A2 phase as shown in Fig. 3 in case of Fe–Ga–Mn in addition to the presence of $L1_2$ phase at the grain boundaries of parent phase, A2, as elucidated in Figs. 4 and 5, for Fe–Ga–Al and Fe–Ga–Ti alloys, respectively.

In Figs. 3, 4, and 5, $L1_2$ phase precipitated at the grain boundaries of A2 phase, in a thin film shape with about 0.25 µm in size.

The size of the microstructure of Ni-doped alloy is the finest one compared to the other microstructures. However, the Ti doped in Fe–Ga alloy own the coarsest microstructure. It noteworthy that the microstructure of Al-doped alloy has a longitudinal gain structure, while in case of Mn and Ti, the microstructure consists of equiaxed poly crystalline structure, as it can be seen in Fig. 1.

Moreover, Golovin et al [18] studied and confirmed the formation of small D03 type ordered clusters in the microstructure of $Fe_{81}Ga_{19}$ alloy. Therefore, the probability of the presence of clusters of the same phase (D03) in the microstructures of the investigated Fe–Ga alloys is very high. With high magnification, the microstructures of the Fe–Ga alloys displayed in Figs. 3, 4, and 5, could contains some ordered clusters of D03 phase.

Figure 6 explains the EDS analysis results of different microstructural features in Fe–Ga–Ni specimen are mentioned: point 1: A2 matrix; and point 2: second phase of $L1_2$. The A2 matrix in this ternary alloy is richer in Ga but leaner in Fe and Ni than in the second-phase $L1_2$ precipitates.

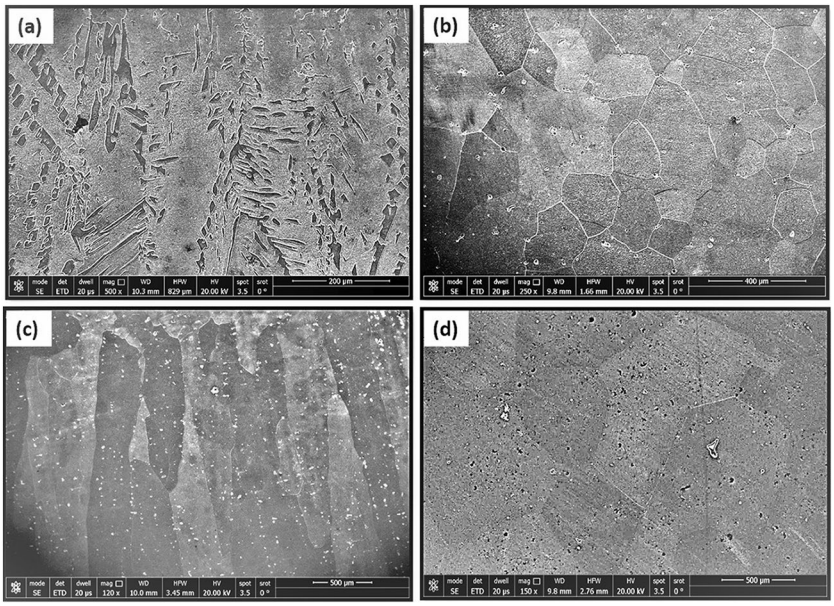

Fig. 1 Microstructure of Fe–Ga alloys with (**a**) Ni, (**b**) Mn, (**c**) Al, and (**d**) Ti elements

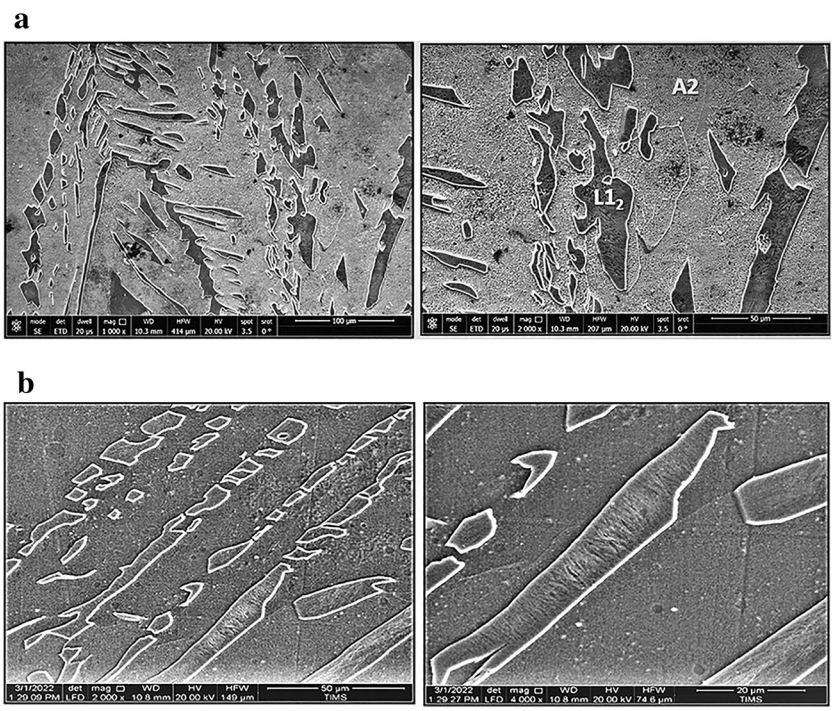

Fig. 2 (**a**) Microstructure of Fe–Ga–Ni alloy with different magnifications. (**b**) Backscattered image of Fe–Ga–Ni specimen's microstructure

To study the distribution of alloying elements in the microstructure of the $Fe_{80}Ga_{15}Ni_5$ alloy, the line scanning analysis technique was applied, as shown in Fig. 7. The differences in micro-chemical analysis for the alloying elements between two phases (A2 and $L1_2$) could hardly be demonstrated. The line scanning analysis go through the $L1_2$ phase as illustrated in Fig. 7, where Fe in blue color, Ga in green color, and Ni in red color.

X ray Diffraction

To recognize and investigate the structure and phases in each sample taken from the Fe–Ga-studied alloys, x-ray diffraction (XRD) measurements were carried out at room temperature. The XRD patterns for the four samples representing Fe–Ga–Ni, Fe–Ga–Mn, Fe–Ga–Al, and Fe–Ga–Ti alloys are shown in Fig. 8. All the XRD reflections were indexed with

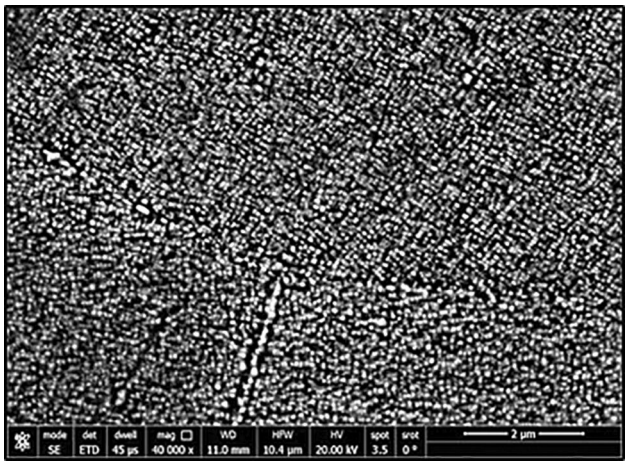

Fig. 3 Microstructure of $Fe_{80}Ga_{15}Mn_5$ specimen

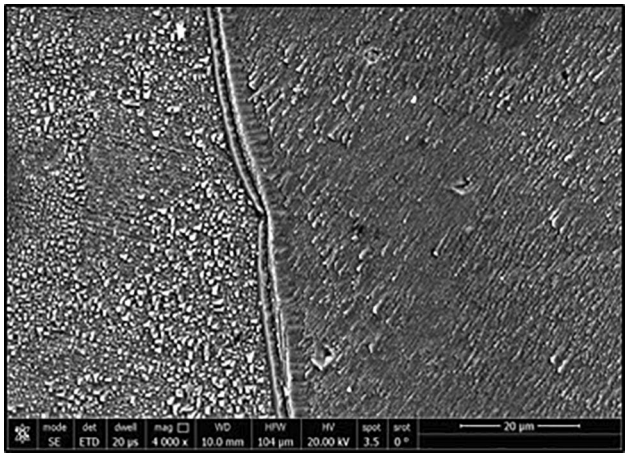

Fig. 4 Microstructure of $Fe_{80}Ga_{15}Al_2$ specimen

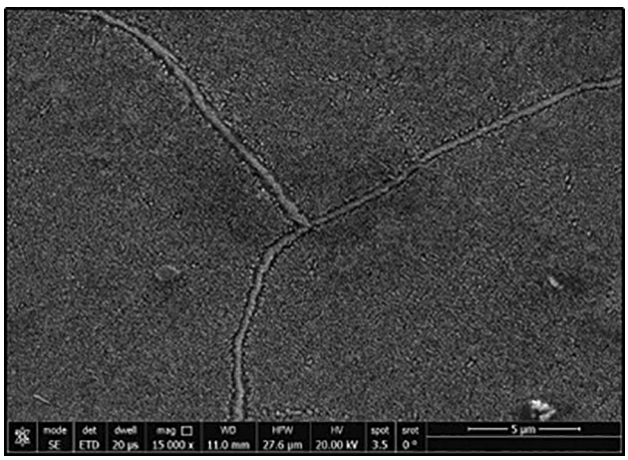

Fig. 5 Microstructure of $Fe_{80}Ga_{15}Ti_5$ specimen

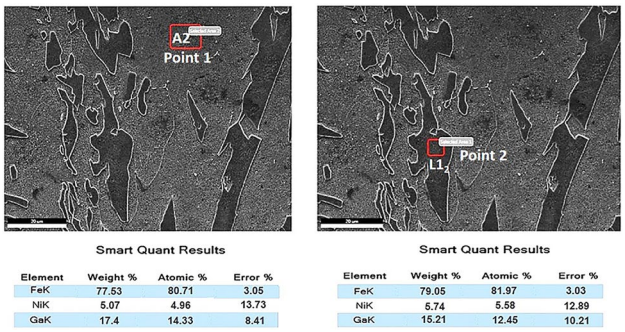

Fig. 6 SEM and EDS for different phase found in $Fe_{80}Ga_{15}Ni_5$ specimen

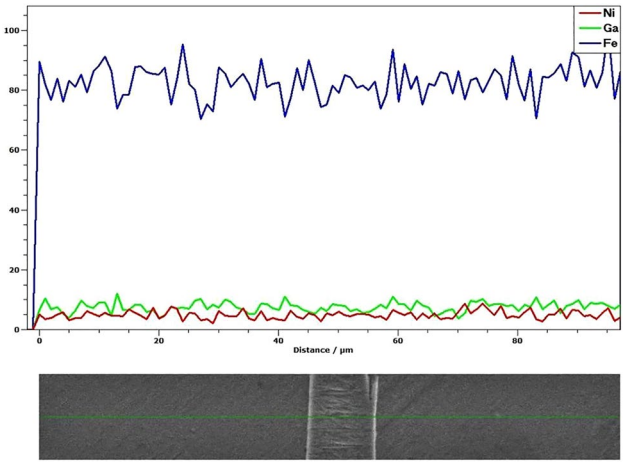

Fig. 7 Line scanning across $L1_2$ phase found in $Fe_{80}Ga_{15}Ni_5$ specimen

the bcc-like structure, the parent phase or matrix, which is the prevailing phase in the microstructure of all investigated alloys. The peaks illustrated in Fig. 7 are indexed to the following planes: (110), which represented the prominent peak, in addition to (200) and (211) planes. These three strongest indexed Bragg reflections for the latter three planes represent the single phase Fe–Ga bcc-like structure defined as a disordered A2 structure from examination of the phase diagram [19–21].

The other phases, such as the cubic order $L1_2$ phase, were hardly detected, according to its lower percentages in the microstructures, and represented by the plan of (111) in the XRD patterns.

Magnetization Properties

The magnetization characterization of the investigated Fe–Ga samples was carried out by the vibrating sample magnetometer (VSM). The plots (hysteresis loops) for the

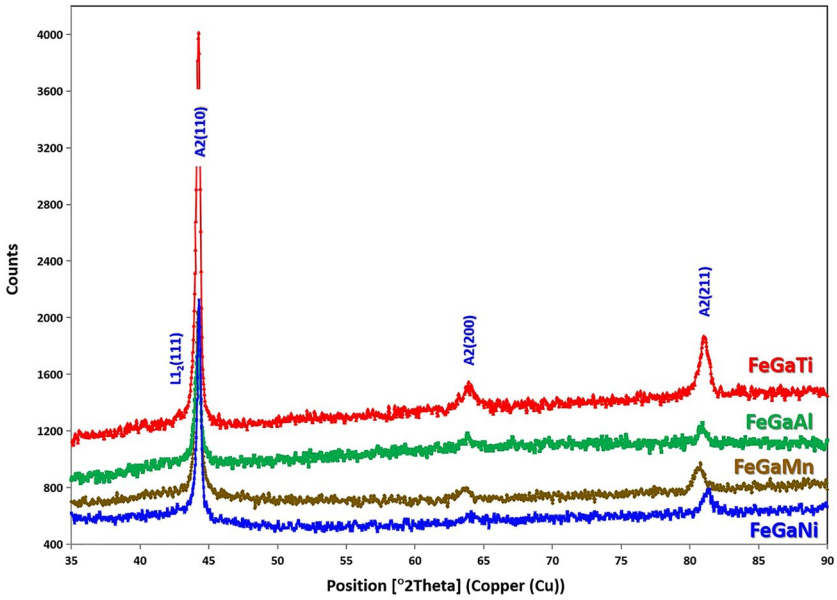

Fig. 8 X-ray diffraction patterns for investigated samples

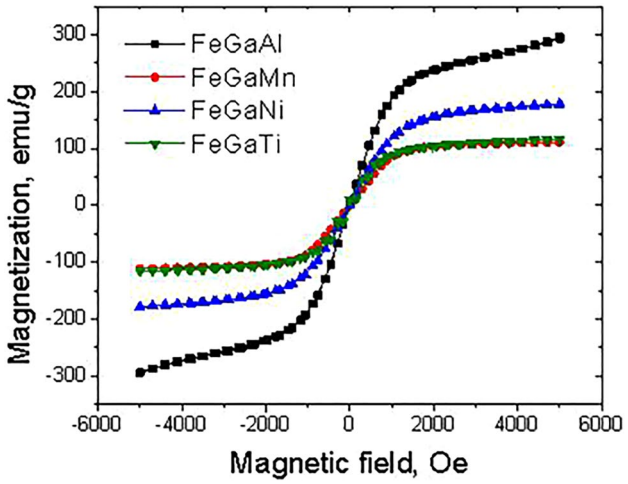

Fig. 9 Effect of the third alloying element on the M-H hysteresis loops of Fe–Ga-Z alloys

magnetization (M) as a function of the applied field (H) for (a) Fe–Ga–Ni, (b) Fe–Ga–Mn, (c) Fe–Ga–Al, and (d) Fe–Ga–Ti alloys are shown in Fig. 9. These magnetization experiments were performed under an applied field of 15 KOe at room temperature.

The saturation magnetization (Ms), remanent magnetization (Mr), and coercivity (Hci) for all the samples used in this study are illustrated in Fig. 10. It can be observed that in comparison with other samples, the sample of Fe–Ga–Al has the highest value of Ms, which is 295.21 emu/g. However, the Fe–Ga–Mn sample obtained the lowest Ms measurement among other investigated samples, equal to 111.23 emu/g, see Fig. 10a. The other two samples of Fe–Ga–Ni and Fe–Ga–Ti gained the Ms values of 178.63 and 116.44 emu/g, respectively. According to the results obtained by Quinn et al., the saturation magnetization (Ms) value of the ferromagnetic $L1_2$ phase is significantly lower than that of the A2 phase [22, 23]. Where there is a clear trend of decreasing magnetization with the appearance of the secondary $L1_2$ phase.

For the Mr and Hci measurements that appeared in Fig. 10b and c, both have the same trend and shape where the sample Fe–Ga–Ti got the maximum values for Mr and Hci then decreased to the minimum amount in case of the Fe–Ga–Al sample. After that, a slight increase in Hci takes place with Fe–Ga–Mn sample. Further increment in both Mr and Hc was obtained with the sample of Fe–Ga–Ni.

It can be concluded that the doping of the Al element in Fe–Ga alloy expands the saturation magnetization of this alloy while decreasing the coercivity to the lowest value in comparison with other alloying elements of Ni, Mn, and Ti, where Al enhances the Ms of Fe–Ga alloy better than Ni, Ti and Mn by about 165%, 250 %, and 265 %, respectively.

Hardness Measurements

To study the influence of adding various third alloying elements such as Ni, Mn, Al, and Ti on the mechanical properties of $Fe_{81}Ga_{19}Z_x$ alloy, hardness property was measured as the fastest, easiest, and most accurate property among other mechanical properties. Table 2 contains the hardness values for the investigated alloys of $Fe_{81}Ga_{14}Ni_5$, $Fe_{81}Ga_{14}Mn_5$, $Fe_{81}Ga_{17}Al_2$, and $Fe_{81}Ga_{14}Ti_5$ alloys.

As elucidated in Table 2, the $Fe_{81}Ga_{14}Ti_5$ alloy has the highest hardness value (481.3 Hv5), while the $Fe_{81}Ga_{17}Al_2$ alloy got the lowest hardness measurement (276.95 Hv5) in comparison with other $Fe_{81}Ga_{19}Z_x$ alloys. The other two

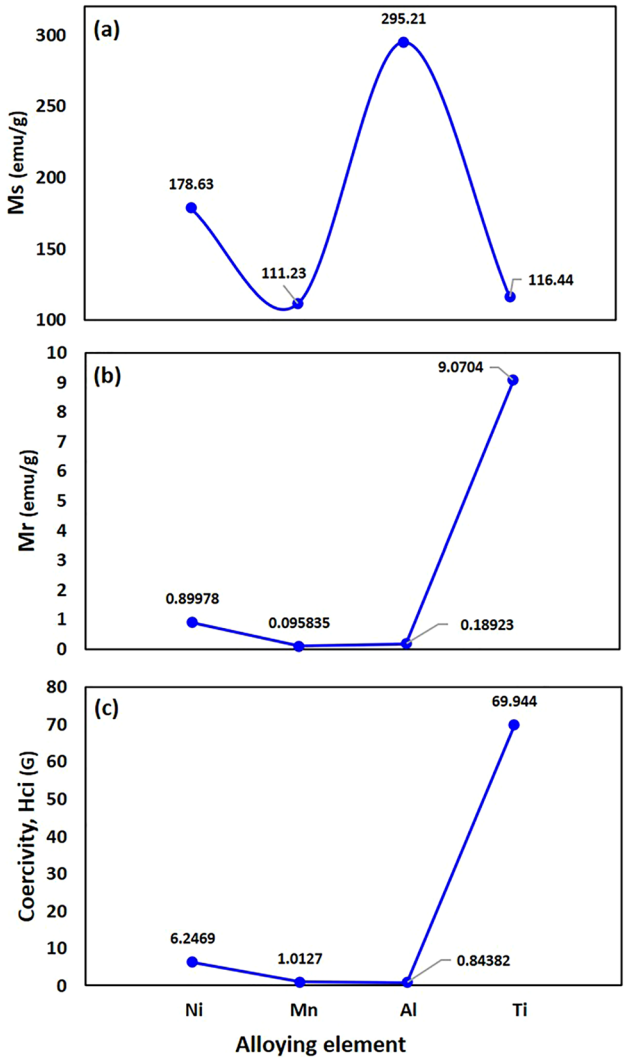

Fig. 10 Influence of the third alloying element on the (**a**) saturation magnetization (Ms), (**b**) remanent magnetization (Mr), and (**c**) coercivity (Hci) of Fe–Ga alloys

Table 2 Hardness measurements for $Fe_{81}Ga_{19}Z_x$ alloys under investigation

Alloy	HV_5
Fe–Ga–Ni	356.2
3-Fe–Ga–Mn	324.5
4-Fe–Ga–Al	276.95
5-Fe–Ga–Ti	481.3

alloys obtained 356.2 and 324.5 Hv5 for $Fe_{81}Ga_{14}Ni_5$ and $Fe_{81}Ga_{14}Mn_5$ alloys, respectively.

The highest hardness value for $Fe_{81}Ga_{19}Z_x$ alloy, which was gained by adding 2 at.% Ti, could be attributed to the precipitation of a second hard phase enriched with Ti element.

Table 3 indicates the microhardness measurements for the phases presented in the microstructure of the Fe81Ga14Ni5

Table 3 Microhardness of phases in $Fe_{81}Ga_{14}Ni_5$ specimen

Phase	HV_{50}
A2	260
$L1_2$	465

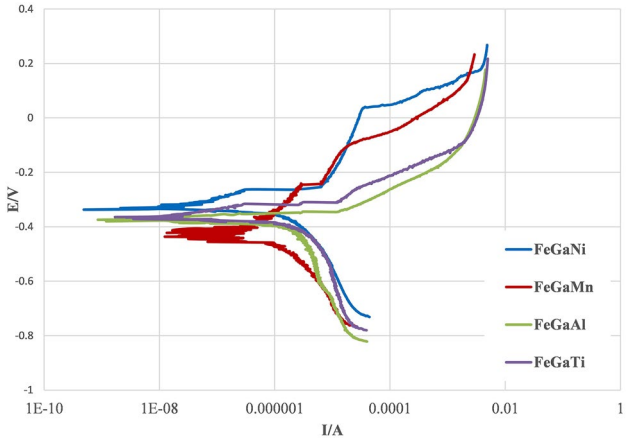

Fig. 11 Tafel curves of the Fe–Ga alloys specimens

specimen, which is A2 and $L1_2$ phases. The microhardness test was measured at room temperature under a load of 50 g. It can be noticed that the $L1_2$ phase is more complicated than the other one, which is the matrix, where A2 phase obtained a microhardness value of 245 Hv, while the $L1_2$ phase has 465 Hv.

Corrosion of Fe–GaX Shape Memory Alloys

It is well known that the corrosion resistance of metallic alloys is very related to their constituting elements and microstructure [24–26]. The investigated alloys are all Fe–Ga-based alloys that differ in the third alloying element (Ni; Mn; Al and Ti). As observed in microstructure section, these different alloying additives resulted in significantly different microstructures. The microstructure morphology of Fe–Ga alloy changed from the very fine structure in the case of Fe–Ga–Ni, to fine globular-grained morphology in Fe–Ga–Mn alloy and changed to coarse longitudinal grains when alloyed with Al while attaining the globular structure again with Ti addition; however, with coarser grain size.

Figure 11 shows the Tafel plots obtained from polarization tests of the different alloys. Fe–Ga–Ni alloy showed an OCP value of (~− 0.33) with a long "constant potential" stage, after which passivation started, and then the passive layer distorted and corrosion continued. Alloy Fe–Ga–Mn recorded a more negative OCP (~ 0.37) and showed behavior close to Fe–Ga–Ni alloy with a much shorter "constant potential" stage and less passivation. Fe–Ga–Al alloy showed the most negative OCP value of − 0.42 with a

longer "constant potential" region, and no passivation was observed. It was corroded continuously without delay, and the corrosion rate increased remarkably by the end of the test. Ti-containing alloy (Fe–Ga–Ti) had OCP of (~ 0.38) and presented a long "constant potential" period, which is almost similar to that of Fe–Ga–Al, and shorter than Fe–Ga–Ni alloy, with a tendency to passivate.

The impedance curves representing the resistance of the different samples are presented in Fig. 12. According to this figure, Fe–Ga–Mn alloy is the most resistant to the corrosive media among all the samples, while Fe–Ga–Al showed the smallest impedance circle. Again, the influence of microstructure features along with alloy composition was significantly affected.

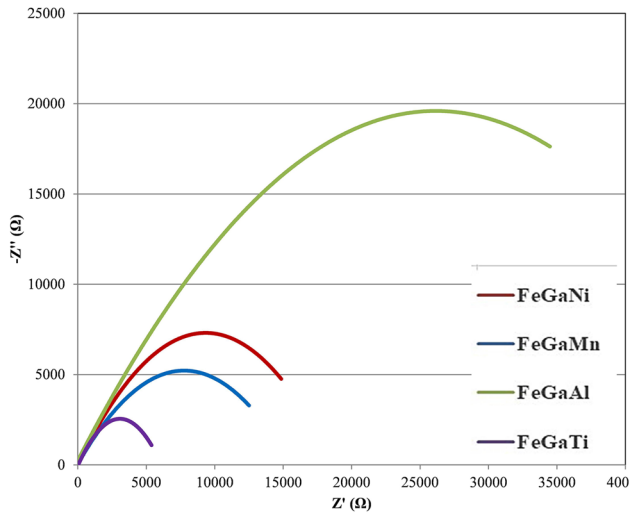

Fig. 12 Impedance plots of the Fe–Ga alloys specimens

The Bod plots represented in Fig. 13 further support the impedance results. Table 4 summarizes the polarization test results of the different alloys.

The polarization resistance and the corrosion rates, as calculated from Tafel curves of Fig. 11, are shown in Table 4. According to this table, Fe–Ga–Mn alloy is the most resistant to the corrosive media among all the samples, considering the lowest corrosion rate ($C_R = 0.03$ mm/year) and highest polarization resistance (Rp = 53 kΩ). Conversely, Fe–Ga–Al showed the lowest value of Rp (8 kΩ) and the highest corrosion rate ($C_R = 0.19$ mm/year).

In order to understand the elemental distribution from inside to outside the corrosion area, EDS was used to analyze the different areas. An example of EDS measurements is shown in Fig. 14, and the points analysis of the different positions for the investigated alloys are summarized in Table 5.

From Fig. 14 and Table 5, it is clear that wt.% Fe decreased inside the corroded area in the Fe–Ga–Ni and

Table 4 Summary of the polarization test measurements

	OCP	Corrosion rate, mm/year	Ecorr, mV	Icorr, μA	Rp, kΩ
Fe–Ga–Ni	− 0.33	0.087	339.8	2.794	22.3
Fe–Ga–Mn	− 0.37	0.03	433.5	1.013	53
Fe–Ga–Al	− 0.42	0.19	392.2	4.04	8
Fe–Ga–Ti	− 0.38	0.14	376	4.58	11.4

Fig. 13 Bod plots of the Fe–Ga alloys specimens

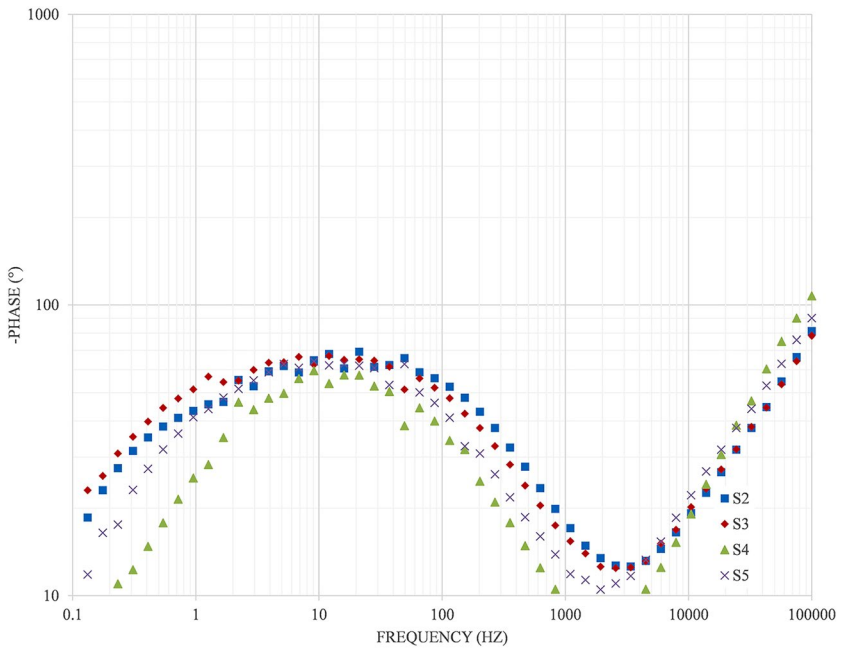

Fe–Ga–Ti alloys while remaining almost unchanged in Fe–Ga–Mn and Fe–Ga–Al alloys. Reversely, Ga increased inside the corroded area in the case of Fe–Ga–Ni and Fe–Ga–Ti alloys, while no changes were observed in its distribution in Fe–Ga–Mn and Fe–Ga–Al alloys. Regarding the third alloying element, Mn decreased in the corroded area while Ni, Al, and Ti increased, indicating the resistance of Mn to corrosion.

To summarize, Fe–Ga–Mn alloy with the fine globular grain structure showed the best resistance to corrosion among the studied alloys. The longer constant potential stage in Fe–Ga–Ni and Fe–Ga–Ti alloys led to low corrosion resistance (polarization resistance is inversely related to the corrosion current).

Fe–Ga–Al alloy with the coarse longitudinal grain structure (Fig. 1c) showed the lowest resistance to corrosion. Besides the long constant potential period, there was no observed passivation for this alloy. Moreover, Zhang et al. [27] showed that the grains' orientation and size are effective in altering the corrosion resistance of the aluminum alloys. Therefore, the shape of the grains in the case of Al alloy significantly decreased its corrosion resistance, most probably via providing a larger grain boundary area for galvanic corrosion.

In Fe–Ga–Ni alloy, although a well-defined passivation occurred, the passive layer was broken, and the sample could not re-passivate further. According to Zhang et al. [28], the inability of alloy to passivate is affected by the existence of second-phase particles that reduce the re-passivation possibility in the surrounding areas, and they also become points of corrosion attack.

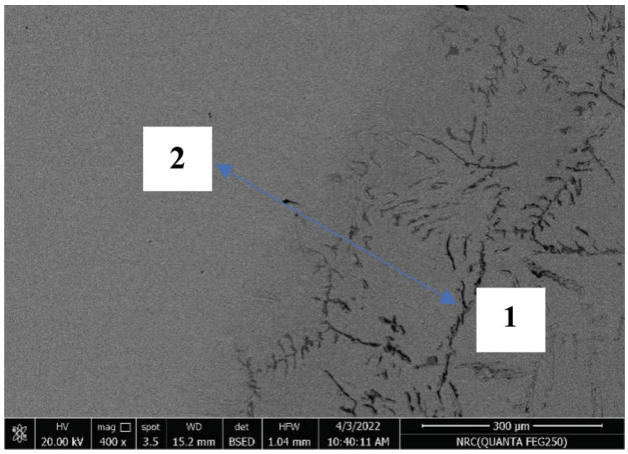

Fig. 14 Example of SEM micrograph for Fe–Ga–Ni sample showing the points at which EDS was carried out where: (1) and (2) representing inside and outside of corroded area, respectively

Table 5 EDS point analysis at (1) inside and (2) outside of the corroded area of (a) Fe–Ga–Ni, (b) Fe–Ga–Mn, (c) Fe–Ga–Al, and (d) Fe–Ga–Ti alloys

(a)

Element	Weight %	Atomic %	Net Int.	Error %
FeK	76.58	79.67	148.25	3.43
NiK	5.17	5.11	6.9	23.92
GaK	18.25	15.21	13.01	17.13

Element	Weight %	Atomic %	Net Int.	Error %
FeK	78.35	81.27	181.85	3.17
NiK	4.79	4.73	7.66	23.56
GaK	16.85	14	14.42	16.87

(b)

Element	Weight %	Atomic %	Net Int.	Error %
MnK	5.14	5.55	13.6	16.29
FeK	64.43	68.53	145.28	3.56
GaK	30.43	25.92	25.51	11.02

Element	Weight %	Atomic %	Net Int.	Error %
MnK	6.21	6.69	15.99	15.87
FeK	64.32	68.25	141.21	3.57
GaK	29.48	25.06	24.08	11.73

(c)

Element	Weight %	Atomic %	Net Int.	Error %
AlK	2.48	5.23	9.11	21.66
FeK	75	76.4	216.05	2.97
GaK	22.52	18.38	24.18	12.06

Element	Weight %	Atomic %	Net Int.	Error %
AlK	2.18	4.61	7.76	24.42
FeK	74.98	76.68	210.19	3.04
GaK	22.85	18.72	23.87	14.46

(d)

Element	Weight %	Atomic %	Net Int.	Error %
TiK	5.42	6.52	23.63	13.3
FeK	75.02	77.33	163.19	3.38
GaK	19.56	16.15	15.98	15.67

Element	Weight %	Atomic %	Net Int.	Error %
TiK	3.63	4.36	17.84	14.94
FeK	78.56	80.94	190.59	3.14
GaK	17.81	14.7	16.19	15.63

Conclusions

1. The microstructure of the investigated $Fe_{81}Ga_{19-x}Z_x$ ($X = 5$ at.% of Ni or Mn or Ti and 2 at.% Al; separately) alloys consists of the A2 phase as a matrix, the bcc-like disordered structure in addition to the $L1_2$ phase, the cubic order structure.
2. The highest saturation magnetization (Ms) measurement was achieved by adding 2 at.% Al to the $Fe_{81}Ga_{19}$ alloy at the expense of Ga. However, $Fe_{81}Ga_{14}Mn_5$ alloy attained the minimum value of Ms compared to other examined alloys.
3. Both remanent magnetization (Mr) and coercivity (Hci) properties reached their peaks with doping 5 at.% of Ti in Fe–Ga alloy. While in the case of using 2 at.% of Al element, the preceding properties were decreased dramatically to the minimum level.
4. $Fe_{81}Ga_{14}Ti_5$ SMA has the maximum value of hardness property that represents the mechanical properties among other investigated alloys. In contrast, $Fe_{81}Ga_{17}Al_2$ SMA got the lowest one.
5. The microhardness of the precipitated $L1_2$ phase is higher than that of the matrix phase, A2 bcc structure, almost about two times.
6. The microstructure of the different samples notably affected their corrosion behavior. Fe–Ga–Mn alloy with the fine globular-grain structure showed the best resistance to corrosion among the studied alloys. On the other hand, Fe–Ga–Al alloy with the coarse longitudinal grain structure exhibited the lowest resistance to corrosion.

Acknowledgments The corresponding author would like to acknowledge Prof. Magdy Kaseem's help in casting the investigation samples.

Funding Open access funding provided by The Science, Technology & Innovation Funding Authority (STDF) in cooperation with The Egyptian Knowledge Bank (EKB).

References

1. A. Emdadi, V.V. Palacheva, V.V. Cheverikin, S. Divinski, G. Wilde, I.S. Golovin, Structure and magnetic properties of Fe–Ga alloys doped by Tb. J. Alloy. Compd. **758**(25), 214–223 (2018)
2. M. Sofronie, B. Popescu, M. Enculescu, M. Tolea, F. Tolea, Processing effects on the martensitic transformation and related properties in the $Ni_{55}Fe_{18}Nd_2Ga_{25}$ ferromagnetic shape memory alloy. Nanomaterials. **12**(20), 3667 (2022). https://doi.org/10.3390/nano12203667
3. M. Ebrahimi, S. Attarilar, C. Gode, S.R. Kandavalli, M. Shamsborhan, Q. Wang, Conceptual analysis on severe plastic deformation processes of shape memory alloys: mechanical properties and microstructure characterization. Metals. **13**(3), 447 (2023). https://doi.org/10.3390/met13030447
4. J. Atulasimha, A.B. Flatau, A review of magnetostrictive iron-gallium alloys. Smart Mater. Struct. **20**(4), 043001 (2011)
5. F. Tolea, B. Popescu, C. Bartha, M. Enculescu, M. Tolea, M. Sofronie, Kinetics and the effect of thermal treatments on the martensitic transformation and magnetic properties in $Ni_{49}Mn_{32}Ga_{19}$ ferromagnetic shape memory ribbons. Magnetochemistry. **9**, 7 (2023). https://doi.org/10.3390/magnetochemistry9010007
6. A. Emdadi, V. Palacheva, V. Cheverikin, AYu. Churyumov, I.S. Golovin, Fe–Ga–Tb alloys for soft magnetic applications. J. Magn. Magn. Mater. **497**, 165987 (2020)
7. D.I. Holsworth, D.L. Du Quesnay, The effects of hot iso-static pressing on the porosity and fatigue properties of Galfenol steels. Int. J. Fatigue. **131**, 105325 (2020)
8. I.S. Golovin, L.Y. Dubov, Y.V. Funtikov, V.V. Palacheva, J. Cifre, D. Hamana, Study of ordering and properties in Fe–Ga alloys with 18 and 21 at. pct Ga. Metall. Mater. Trans. A. **46**, 1131–1139 (2015)
9. Y. Li, D. Zhao, J. Liu, Giant and reversible room temperature elastocaloric effect in a single-crystalline Ni–Fe–Ga magnetic shape memory alloy. Sci. Rep. **6**, 25500 (2016). https://doi.org/10.1038/srep25500
10. N.L. Raveendran, R. Pandian, S. Murugesan, K. Asokan, R.R. Kumar, Phase evolution and magnetic properties of DC sputtered Fe–Ga (Galfenol) thin films with growth temperatures. J. Alloys Compd. **704**, 420–424 (2017)
11. O.O. Pavlukhina, V.V. Sokolovskiy, M.V. Matyunina, M.A. Zagrebin, O.N. Miroshkina, D.R. Baigutlin, V.D. Buchelnikov, A.K. Mohamed, V.V. Palacheva, V.A. Palachev, A.M. Balagurov, I.S. Golovin, Phase transitions in Fe-(23–24) Ga alloys: experimental results and modeling. J. Alloys Compd. **885**(4), 160917 (2021)
12. I.S. Golovin, V.V. Palacheva, A.K. Mohamed, A.M. Balagutov, Structure and properties of Fe–Ga alloys as promising materials for electronics. Phys. Metals Metallogr. **121**(9), 851–893 (2020)
13. T.V. Jayaraman, N. Srisukhumbowornchai, S. Guruswamy, M.L. Free, Corrosion studies of single crystals of iron–gallium alloys in aqueous environments. Corros. Sci. **49**(10), 4015–4027 (2007)
14. I.S. Golovin, V.V. Palacheva, A.I. Bazlov, J. Cifre, J. Pons, Structure and anelasticity of Fe_3Ga and Fe_3 (Ga, Al) type alloys. J. Alloys Compd. **644**, 959–967 (2015)
15. H. Liu, Z.Z. Zhang, Y.J. Wu, L.M. Dong, H.O. Wang, M.X. Cao, W.S. Tan, Effect of Ni doping on the microstructure and magnetic properties of Fe–Ga ribbons. J. Mater. Sci. Mater. Electron. **30**, 18780–18787 (2019)
16. X. Sun, D. Cong, Y. Ren, K.-D. Liss, D.E. Brown, Z. Ma, S. Hao, W. Xia, Z. Chen, L. Ma, X. Zhao, Z. He, J. Liu, R. Li, Y. Wang, Magnetic-field induced strain-glass-to-martensite transition in a Fe–Mn–Ga alloy. Acta Mater. **183**, 11–23 (2020)
17. O. Örnek, A. İyigör, A.S. Meriç, M. Çanlı, M. Özduran, N. Arıkan, First-Principle investigations of (Ti1–x V x) 2FeGa alloys.

A study on structural, magnetic, electronic, and elastic properties. Russ. J. Phys. Chem. A. **95**(13), 2592–2599 (2021)
18. I.S. Golovin, A.M. Balagurov, W.C. Cheng, J. Cifre, D.A. Burdin, I.A. Bobrikov, V.V. Palacheva, N. Yu Samoylova, E.N. Zanaeva, In situ studies of atomic ordering in Fe-19Ga type alloys. Intermetallics. **105**, 6–12 (2019). https://doi.org/10.1016/j.intermet.2018.10.029
19. C. Bormio-Nunesa, F.M. Cardoso, Assessment of Fe–Ga–B alloy magnetomechanical behavior. J. Mater. Res. **33**(15), 2207–2213 (2018)
20. T.A. Lograsso, E.M. Summers, Detection and quantification of $D0_3$ chemical order in Fe–Ga alloys using high resolution X-ray diffraction. Mater. Sci. Eng. A. **416**, 240–245 (2006)
21. R.A. Laroche, S. Guruswamy, Quantitative determination of short-range order in magnetostrictive Fe-12.5 at.% Ga alloy single crystals. AIP Adv. **10**, 095203 (2020). https://doi.org/10.1063/5.0019213
22. C.J. Quinn, P.J. Grundy, J. Mellors, The structural and magnetic properties of rapidly solidified $Fe_{100-x}Ga_x$ alloys, for $128 \leq x \geq 275$. J. Magn. Magn. Mater. **361**, 74–80 (2014). https://doi.org/10.1016/j.jmmm.2014.02.004
23. P. Taheri, Design, processing, and characterization of mechanically alloyed galfenol & lightly rare earth doped FeGa alloys as smart materials for actuators and transducers, Doctor of Philosophy, (December 2016)
24. T.S. Sidhu, A. Malik, S. Prakash, R.D. Agrawal, Cyclic oxidation behavior of Ni-and Fe-based superalloys in air and Na_2SO_4-25% NaCl molten salt environment at 800 °C. Afr. J. Phys. **8**(4), 1–7 (2021)
25. I.M.C. Bopape, E.N. Ogunmuyiwa, M.B. Shongwe, Effect of Co and Fe contents on the microstructure and corrosion behavior of heat-treated Ni-Fe–Co superalloys in 3.5 wt.% NaCl aqueous solution. Int. J. Adv. Manuf. Technol. **119**, 301–287 (2022). https://doi.org/10.1007/s00170-021-08111-1
26. N. El-Bagoury, M.A. Amin, Q. Mohsen, Effect of various heat treatment conditions on microstructure, mechanical properties and corrosion behavior of Ni base superalloys. Int. J. Electrochem. Sci. **6**(12), 6718–6732 (2011)
27. J. Zhang, X. Ding, R. Chen, J. Zhang, Corrosion behaviors of hot-extruded $Mg_{96}Y_2Zn_2$ alloy in transverse and longitudinal directions: guidance for parameters selection. J. Alloy. Compd. **923**, 166405 (2022)
28. Da. Zhang, J. Dong, J. Xiong, N. Jiang, J. Li, W. Guo, Microstructure characteristics and corrosion behavior of refill friction stir spot welded 7050 aluminum alloy. J. Market. Res. **20**, 1302–1314 (2022)